Magnetohydrodynamical Effects on Nuclear Deflagration Fronts in Type Ia Supernovae

Boyan Hristov[1,2], David C. Collins[2], Peter Hoeflich[2], Charles A. Weatherford[1], and Tiara R. Diamond[3]
[1] Department of Physics, Florida A&M University, Tallahassee, FL 32301, USA
[2] Department of Physics, Florida State University, Tallahassee, FL 32306, USA
[3] NASA Goddard Space Flight Center, Greenbelt, MD 20771, USA

Abstract

This article presents a study of the effects of magnetic fields on non-distributed nuclear burning fronts as a possible solution to a fundamental problem for the thermonuclear explosion of a Chandrasekhar mass (M_{Ch}) white dwarf (WD), the currently favored scenario for the majority of Type Ia SNe. All existing 3D hydrodynamical simulations predict strong global mixing of the burning products due to Rayleigh–Taylor (RT) instabilities, which contradicts observations. As a first step toward studying the flame physics, we present a set of computational magnet-hydrodynamic models in rectangular flux tubes, resembling a small inner region of a WD. We consider initial magnetic fields up to 10^{12} G of various orientations. We find an increasing suppression of RT instabilities starting at about 10^9 G. The front speed tends to decrease with increasing magnitude up to about 10^{11} G. For even higher fields new small-scale, finger-like structures develop, which increase the burning speed by a factor of 3 to 4 above the field-free RT-dominated regime. We suggest that the new instability may provide sufficiently accelerated energy production during the distributed burning regime to go over the Chapman–Jougey limit and trigger a detonation. Finally, we discuss the possible origins of high magnetic fields during the final stage of the progenitor evolution or the explosion.

Key words: instabilities – magnetic fields – magnetohydrodynamics (MHD) – turbulence – white dwarfs

1. Introduction

Type Ia supernovae (SNe Ia) are spectacular explosions at the ends of the lives of stars. Similar explosion energies, spectra, light curves (LC), and LC decline rates, Δm_{15}, established them as standard candles capable of measuring the Universe at the largest cosmological scales (Phillips 1993). Attempts to calibrate a brightness-decline relation began as early as Pskovskii (1977). Recently, Li et al. (2003, 2011), Foley et al. (2013), and Howell et al. (2006) identified the Iax and the super-Chandrasekhar mass subclasses, which further complicates our understanding of these objects. A robust predictive model of SNe Ia first principles is in order.

It is widely accepted that an SN Ia is a thermonuclear explosion resulting from a binary system, of which one star is necessarily a degenerate carbon-oxygen (C–O) white dwarf (WD) (Hoyle & Fowler 1960) near the Chandrasekhar mass (M_{Ch}). Current research considers various progenitor configurations and final outcomes. Depending on whether or not both stars are WDs, the progenitor system is called double-degenerate (DD) or single-degenerate (SD). In addition to progenitor configuration, proposed scenarios are distinguishable by the ignition mechanism and other characteristics. In the case of a DD progenitor system, a dynamical merger or a violent collision between the WDs is capable of releasing enough heat to trigger an ignition. This process can end up as a SN Ia, a highly magnetized WD (MWD), or an accretion-induced collapse (AIC; Iben & Tutukov 1984; Webbink 1984; Benz et al. 1990; Rasio & Shapiro 1994; Segretain et al. 1997; Yoon et al. 2007; Lorén-Aguilar et al. 2009; Wang et al. 2009a, 2009b; Isern et al. 2011; Pakmor et al. 2011). Another class of SNe Ia scenarios is the double-detonation of a sub-M_{Ch} WD with accretion from a helium (He) companion. A detonation in the surface helium layer causes a secondary detonation in the core (Weaver & Woosley 1980; Nomoto 1982a;

Livne 1990; Woosley & Weaver 1994; Hoeflich & Khokhlov 1996; Kromer et al. 2010; Woosley & Kasen 2011). Finally, there is the M_{Ch} explosion scenario, where the WD progenitor accretes material from a companion star and nuclear surface burning to C/O leads to an increase of the WD mass. With increasing WD mass the electron gas in the central region becomes increasingly relativistic, which leads to faster compressional heat release, the rising of the central temperatures, and the triggering of a central C/O deflagration front when the mass of the progenitor approaches M_{Ch}. (Hoyle & Fowler 1960; Sugimoto & Nomoto 1980; Nomoto 1982b; Hoeflich & Stein 2002; Piersanti et al. 2003). It is likely that the dynamical merger, M_{Ch} explosion, and double-detonation channels all contribute to the SN Ia population because of the "stellar amnesia" effect (Hoeflich (2006), and references therein). This can happen in either a SD system, where the donor star is a main-sequence star, a red giant, etc., or in a DD system with another WD being the donor (Whelan & Iben 1973; Piersanti et al. 2003).

In this paper, we will focus on the M_{Ch} explosion channel because of its consistency with a wide range of observations and their statistical properties. From observations we learn that the ejecta of a typical SNe Ia are made of chemical layers (e.g., Barbon et al. 1990; Kirshner et al. 1993; Hoeflich 1995; Fisher et al. 1997; Hoeflich et al. 2002; Marion et al. 2003; Stehle et al. 2005; Tanaka et al. 2011). The overall density structure shows only small deviations from spherical geometry based on the continuum polarization (Howell et al. 2001; Maund et al. 2010; Patat et al. 2012) and based on close to spherical supernovae remnants (Rest et al. 2005; Badenes et al. 2006; Fesen et al. 2007; Rest et al. 2008).

Despite the success of M_{Ch} explosions, there are serious problems related to mixing by the Rayleigh–Taylor (RT) instability during deflagration burning, prior to the phase of strong expansion. This instabilty results in strong large-scale mixing of the ejecta (Khokhlov 1995; Niemeyer &

Hillebrandt 1995; Livne 1999; Reinecke et al. 1999; Gamezo et al. 2003; Röpke et al. 2006; Plewa 2007). Although a layered chemical structure is partially restored during the detonation phase (Gamezo et al. 2005; Röpke et al. 2012), the predicted imprint of deflagration mixing is in contradiction to observations. Several observations of local SNe Ia strongly suggest that a process is necessary to partially suppress the dominant role of RT instabilities during the deflagration:

(a) Direct imaging of the SNR s-Andromeda shows a large "Ca-free" core, indicative of high-density burning and limited mixing (Fesen et al. 2007, 2015).
(b) Spectral fits to observations of post-maximum spectra in normal-bright and subluminous SNe Ia are significantly degraded by injection of radioactive material into the S/Si layer (Figures 12 and 14 in Hoeflich et al. 2002).
(c) Flat-topped or stubby line profiles 1–2 years after the explosion indicate stable isotopes remain near the center after the initial phase of burning (Hoeflich et al. 2004; Motohara et al. 2006; Maeda et al. 2010, 2011; Penney & Hoeflich 2014; Stritzinger et al. 2014; Diamond et al. 2015). This is contrary to the mixing that would occur if RT fully developed.

Good agreement has been obtained with spherical models, whereas the flame physics is inherently multi-dimensional, which causes extensive mixing and strongly degrades individual fits and statistical properties. For a detailed discussion, see Höflich et al. (2006) and Hoeflich et al. (2017).

Had there been a mechanism to suppress the RT instabilities in the early stages of the explosion, these discrepancies would be resolved. This requires a new piece of physics that has previously been left out by the current multi-dimensional models for the deflagration phase. High magnetic fields have been suggested as a solution (Hoeflich et al. 2004; Remming & Khokhlov 2014; Hristov et al. 2016). Several points support this suggestion.

(a) From both theory and simulation, tension in the magnetic field suppresses RT instabilities parallel to the field and also secondary instabilities perpendicular to the field (Chandrasekhar 1961; Stone & Gardiner 2007a, 2007b).
(b) Magnetic surface fields in a wide range of strengths have been observed in WDs (Liebert et al. 2003; Kawka et al. 2007; Giammichele et al. 2012; Kepler et al. 2013, 2016; Sion et al. 2014; Ferrario et al. 2015). While these observations indicate small fields, stronger fields are possible both within the core of the WD and at shorter timescales before the explosion (see Section 4).
(c) Positron transport effects on light curves and spectral line profiles are expected at late times for explosions without magnetic fields (e.g., Milne et al. 1999; Penney & Hoeflich 2014). However, these were not seen in SN2011fe and SN2014j, which were observed for some three years past maximum light (Kerzendorf et al. 2017; Yang et al. 2017).
(d) Penney & Hoeflich (2014) used late-time, near-infrared line profiles to estimate magnetic fields. Though the number of SNe Ia with late-time IR spectra is small, recent observations strongly suggest that initial high magnetic fields with strengths, $B > 10^6$ G are common (Hoeflich et al. 2004; Penney & Hoeflich 2014; Diamond et al. 2015), even assuming fields on small scales comparable to the pressure scale height of the WD.

Table 1
Model (Run) Names, Characterized by the Size and Orientation of the Initial B-field

Initial Magnitude (Gauss)	Initial Direction		
	$B \parallel \hat{y}$	$B \parallel \widehat{yz}$	$B \parallel \hat{z}$
1.4×10^{12}	Y12	YZ12	Z12
1.4×10^{11}	Y11	YZ11	Z11
1.4×10^{10}	Y10	YZ10	Z10
3.5×10^{9}	Y9	YZ9	Z9
3.5×10^{8}	Y8	YZ8	Z8
0	$B = 0$	$(B = 0)$	$(B = 0)$

Note. The front propagates in the $\hat{z}$ direction opposite to the gravitational acceleration, g. Figures 1 and 2 follow the same layout.

The effects of magnetic fields on the nuclear burning in SNe Ia and in a stellar context have been studied in previous works. Potekhin & Chabrier (2012) investigate the effects of magnetic fields on non-resonant thermonuclear reactions in the interiors of C–O WDs. Kutsuna & Shigeyama (2012) study laminar flames in magnetic fields at densities that are typical for a M_{Ch} WD. Ji et al. (2013) simulated a MWDs merger on an axisymmetric cylindrical (2D) domain, followed by Zhu et al. (2015) in full 3D, who obtained final fields of $>10^{10}$ G. Ghezzi et al. (2001, 2004) employed 1D semi-analytic flame models and found that the flame speed is affected by suppression of RT instabilities and additionally studied the asymmetries of a deflagration front in a WD with a large-scale dipole field.

Theories about the origin of WD magnetic fields and in support of amplification of the fields during different stages of the star or the binary system evolution are discussed in the final section.

The article is organized as follows. We describe our method in Section 2. starting with arguments about our choices of magnetic field strength and topology, the initial conditions and boundary conditions, and the regime of burning. The base magnetohydrodynamic (MHD) code, Enzo, is outlined in Section 2.2 and the newly added nuclear reaction model in Section 2.3. Our results are presented in Section 3. In Section 4, we discuss the results, as well as future work and current dynamo theories. The latter is not part of this study, but is important to justify the use of high magnetic fields in the central region of the WD. All equations are written in the *cgs* system of units. Other units are used in plots and throughout the text on occasion.

2. Method

To investigate the effects of magnetic fields on the nuclear burning we ran 16 models identical in all but the magnitude and direction of the initial magnetic field. These runs are listed in Table 1. One model has no magnetic field and the rest are initialized with a uniform magnetic field covering 5 orders of magnitude between 10^8 G to 10^{12} G, and vary between 3 directions: perpendicular to the WD radius, parallel to the WD radius. and at $45°$, respectively labeled $\hat{y}$, $\hat{z}$, and $\widehat{yz}$. The main results can be seen in Figures 1 and 2. Figure 1 shows the burned fraction for projections along $\hat{y}$ (panel a) and $\hat{x}$ (panel b). Columns denote initial field orientation, and rows denote initial field strength. Figure 2 shows the burning rate for each snapshot. These figures are at $t = 0.6$ s. The bottom plot shows the position of the burning front in the computational domain. These will be discussed further in Section 3. To ensure
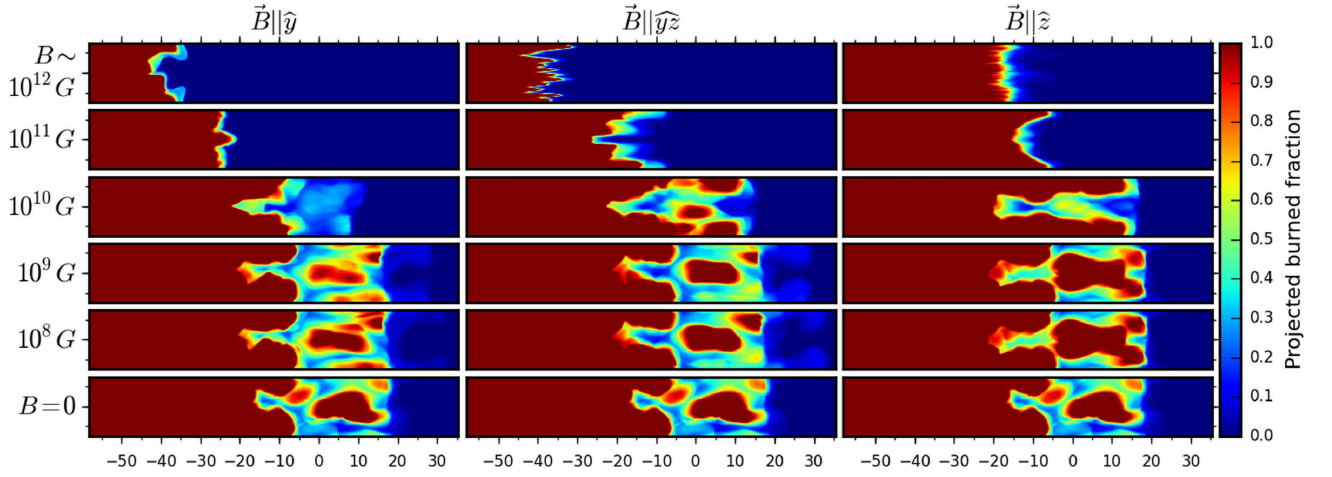
(a) Fuel molar fraction at $t = 0.6$ s projected along the y-axis.
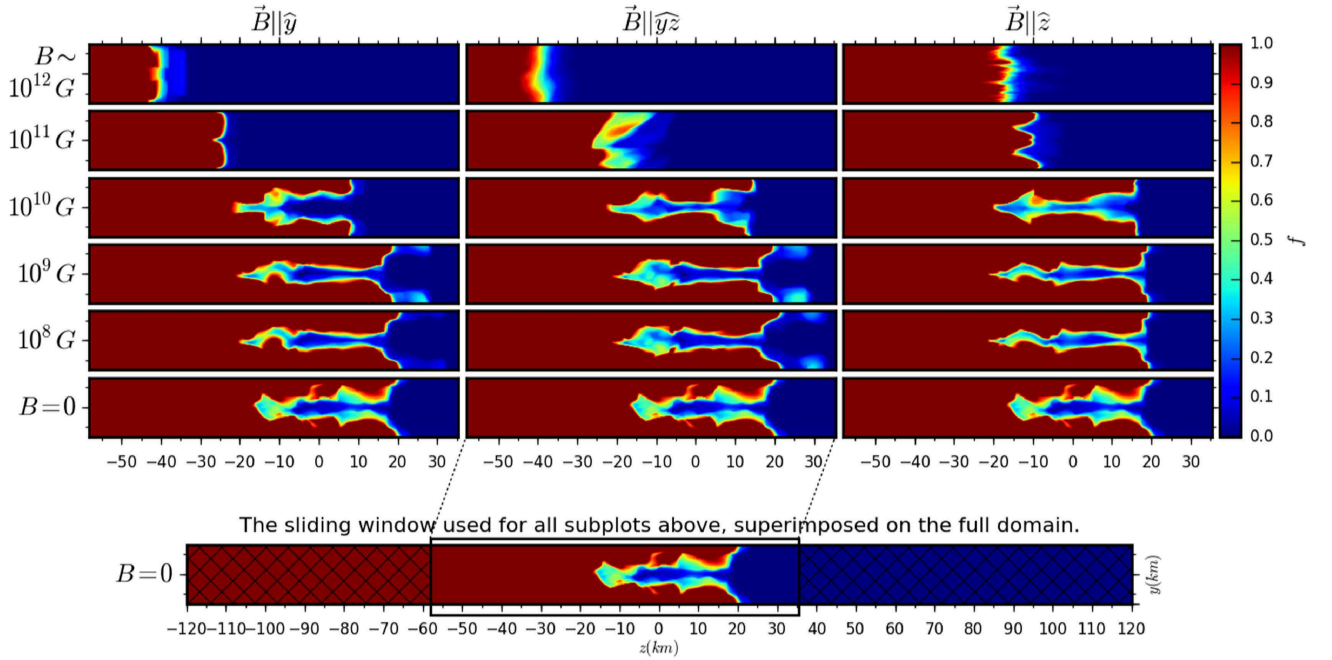
(b) Fuel molar fraction at $t = 0.6$ s projected along the x-axis.

Figure 1. Effects of B on the nuclear burning front. At low or no field (bottom row and up) there is little difference in the behavior. Turbulence dominates and cusps of fuel appear. For models with $B_0 = 10^{10}$ G one can see some stabilization effects of the front, most notably in Y10. For models Y11 and Y12, where the field is in the plane of the front, the front becomes laminar. For models YZ12 and Z12, the strong-field models with a component of the field in the direction of the propagation, we see another change in the burning properties. Smaller modes along z appear where the burning is accelerated. The modes are stabilized by the strong magnetic field. As a result, the fuel burns at a higher rate. We suggest that this may be a mechanism to accelerate the front over the Chapman–Jougey limit and trigger a transition to detonation. See also Figure 2.

the results are insensitive to the boundary, an additional simulation was executed based on model YZ10, but with twice the length of the domain. This longer domain did not change the results. We note that the width of the domain imposes a maximum length of the possible modes, which in turn allows for the existence of a sufficient magnetic field suppressing all linear perturbations (see, for example, the discussion in Stone & Gardiner 2007b).

2.1. White Dwarf Setup

Our work is in the context of an MWD undergoing a M_{Ch}-scenario explosion. Model parameters were chosen to resemble the physical conditions of a WD after the onset of the

deflagration stage, long enough for RT instabilities to set up and while the burning is still in the non-distributed regime.

As this is our first exploration of the impact of magnetic fields on WD, we use a simplified picture in order to understand the physics of the burning front in the presence of a magnetic field. We use rectangular tubes with an initially uniform magnetic field, embedded in the inner region of a WD (Figure 3). We solve the models numerically using full 3D ideal MHD with non-distributed nuclear burning.

2.1.1. Magnetic Field Magnitude

We consider B magnitudes up to 10^{12} G, which is close to those for a virialized WD at 10^{13}–10^{14} G (Alvear Terrero
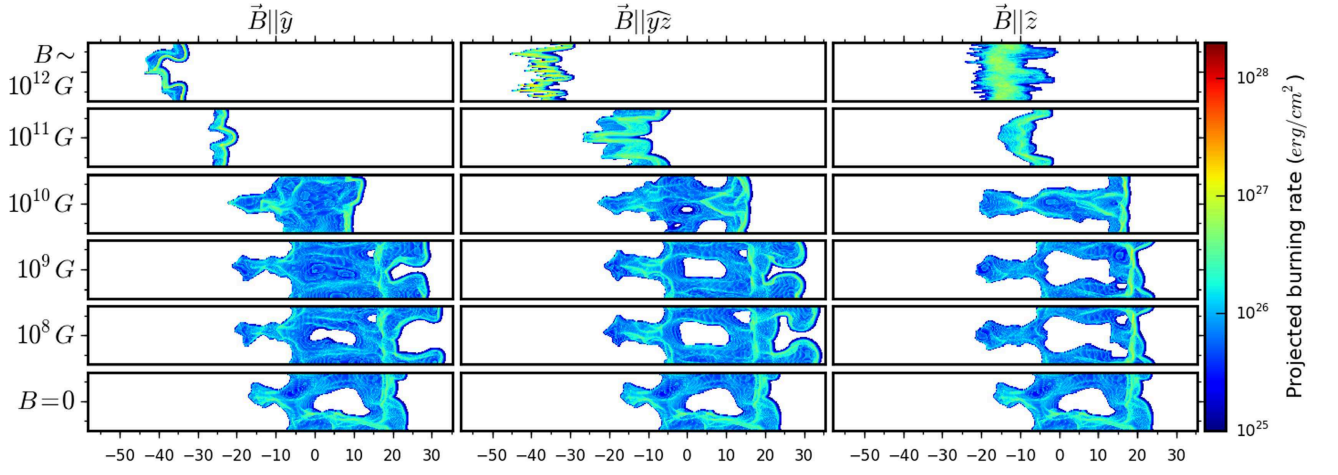
(a) Energy production density rate projected along the y-axis.
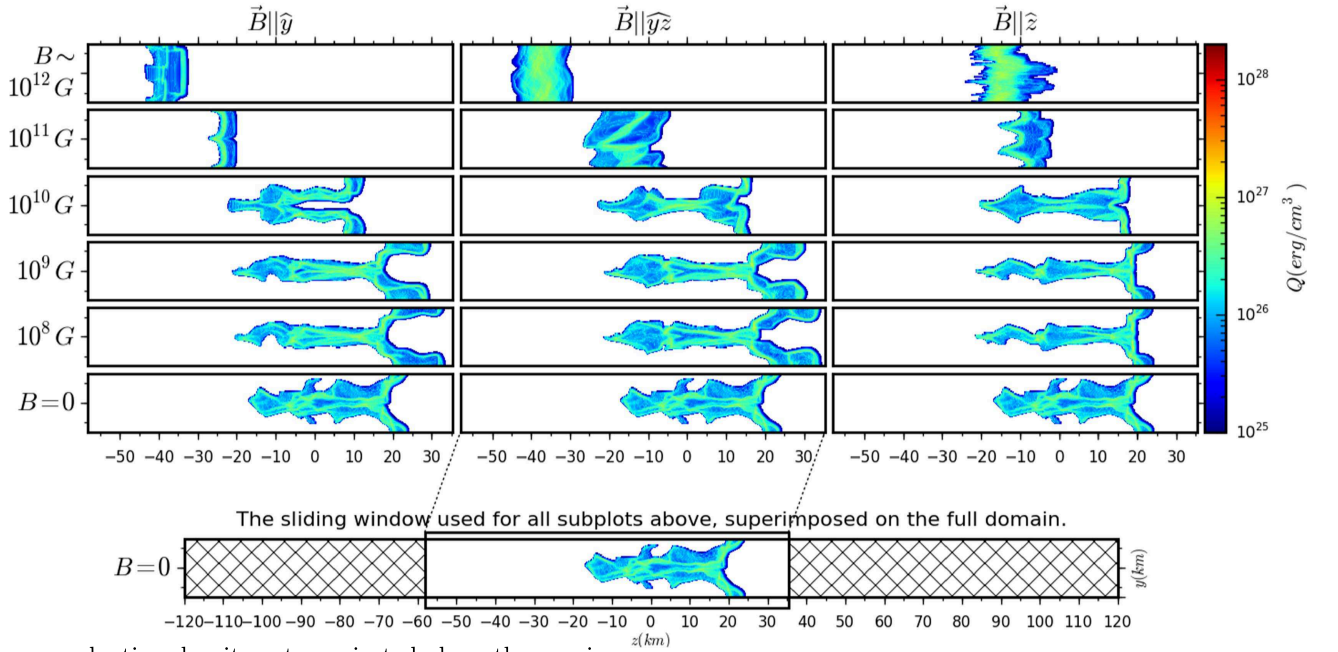
(b) Energy production density rate projected along the x-axis.

Figure 2. Energy production density rate projections at $t = 0.6$ s. See also Figure 1.
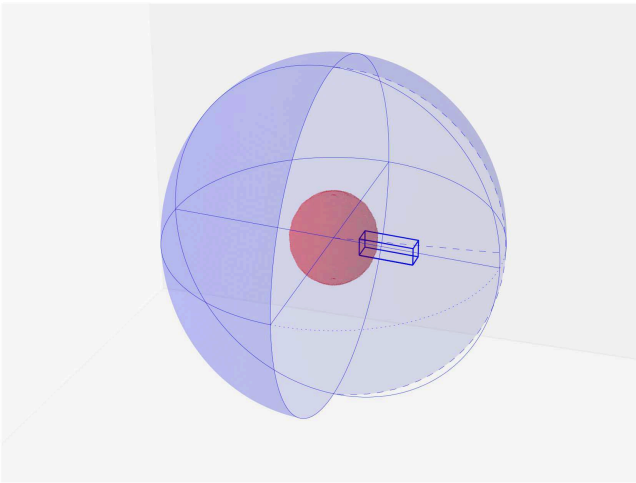
Figure 3. Sketch of the location of our flux tube within the white dwarf. This is close to the center, in the regime of non-distributed burning. See Section 2.1.3 for more details.

et al. 2015; Franzon & Schramm 2017). As an order-of-magnitude estimate of the field strength, we can equate magnetic energy with gravitational binding energy. For a density of $\rho = 10^8$ g cm^{-3} and a radius of 1600 km, using a binding energy of GM^2/R and magnetic energy of B^2R^3, one finds a field strength of 4×10^{12} G.

MWDs are commonly observed in the magnitude range 10^3–10^9 G (Liebert et al. 2003; Kawka et al. 2007; Giammichele et al. 2012; Kepler et al. 2013; Sion et al. 2014; Kepler et al. 2016), where the observations suggest a real cutoff at the upper bound and a sensitivity-limited lower bound (Ferrario et al. 2015). However, these observations are of non-exploding WDs, and the observed magnetic field magnitudes are only on the surface of the WD. Here, we want to model a region close to the center and after a central ignition has occurred, which is a regime not probed by these observations. Small-scale dynamo theory, as well as virial analysis, suggest that fields as large as 10^{12}G are possible in the conditions expected before the explosion. This will be discussed further in Section 4.2.

2.1.2. Field Morphology Considerations

Field morphology can become very complex, as predicted by theory and observations (see Reinsch et al. 2005, and the discussion therein). It is also uncertain whether the field is a dipole (or a multipole) on a large scale or turbulent, or if there is a combination of fields at different scales. We try to accommodate both cases by considering the order of the typical turbulent eddy, $l_{turb} \sim 100$ km, established in Hoeflich & Stein (2002). Furthermore, the domain needs to be long enough to allow the advancement of the burning front for about a second, as well as to make the boundary effects remote enough. With this in mind we made our computational domain $240 \times 15 \times 15$ km ($1024 \times 64 \times 64$ computational zones, see also Section 2.1.4).

2.1.3. Initial and Boundary Conditions

Immediately after a central ignition, RT instabilities would not develop because close to the center of the WD the gravitational acceleration, $g \simeq 0$. We need to pick a later time when the burning front becomes RT-unstable. In addition we are interested in the early evolution of the WD, because plumes created early on have the most time to rise and therefore would create the most mixing. Such conditions are realized in a model in Hoeflich (2006) at time $t = 0.1$ s when the burning front has reached about 1700 km from the center of the WD. At that time and location g and ρ change little within the span of the domain, L_z, so we initialize them with constants $g = 1.9 \times 10^9$ cm s^{-2} and $\rho_0 = 10^8$ g cm^{-3}. Additionally, we keep $\boldsymbol{g}$ constant in time.

We place the burning front at 10 km from the bottom and perturb its plane, so the initial front surface is described by $\zeta(x, y)|_{t=0} = A_0(\cos(k_0 x)) + \cos(k_0 y)$, where $k_0 = 2\pi/\lambda_0$. For all simulations, $A_0 = 5 \times 10^4$ cm and $\lambda_0 = 4.8 \times 10^5$ cm. We initialize the region below the burning front with completely burned material and the one above with unburned fuel. Both regions have the same uniform initial density of $\rho_0 = 10^8$ g cm^{-3}. The initial specific internal energy is also uniform yet different on both sides of the burning front, 3.3×10^{18} and 0.4×10^{18} erg g^{-1} in the burned and unburned regions, respectively, corresponding to initial pressures of 8.25×10^{26} and 10^{26} dyn cm^{-2}. The initial velocity is zero everywhere.

2.1.4. Non-distributed Regime of Burning

At the burning front, with temperatures of $T \gtrsim 10^{9.5}$ K and densities of $\rho_0 \approx 10^8$ g cm^{-3}, the laminar front thickness drops to the order of centimeters: $l_{flame} \sim 10^{-2}$–10 cm (Timmes & Woosley 1992). This is much smaller than other length scales at which an attempt to capture the details of the burning front would make a formidable computational task. As a consequence, and with the burning being complete in this regime, we cannot resolve any intermediate isotopes but only fuel and burning products. We need a grid resolution, Δx, small enough to reproduce accurate MHD features, but much coarser than the front scale length, $\Delta x \gg l_{flame}$, and we use one similar to the resolution in Khokhlov (1995; see Section 2.1.2).

We chose a laminar front speed of 10 km s^{-1} (also after Khokhlov 1995), which is slightly higher than the velocity in Timmes & Woosley (1992). Additionally we used a quasi-1D model to measure the numerical laminar front thickness and speed. This model is similar to the B0 model, except that there

is no perturbation of the initial burning front surface, nor any gradient in initial pressure (10^{26} dyn cm^{-2} everywhere). The results from this simulation confirmed that the model laminar velocity is 10 km s^{-1}. Furthermore, the flame thickness in our simulation is stretched over 4-5 computational zones (about 1 km), which is typical for shock-capturing schemes.

2.2. Code

For the data presented in this paper, we solve the ideal MHD equations with nuclear burning using the adaptive mesh refinement (AMR) code Enzo (Bryan et al. 2014) extended to MHD by Collins et al. (2010). The nuclear burning is a new addition to the code, and described in Section 2.3. The MHD solver uses the hyperbolic solver of Li et al. (2008), the isothermal HLLD Riemann solver developed by Mignone (2007), and the Constrained Transport (CT) method of Gardiner & Stone (2005). The simulations presented here were run with fixed resolution. Enzo has been used in a diverse array of astrophysical settings, including star formation (Abel et al. 2002; Collins et al. 2012), supersonic turbulence (Kritsuk et al. 2007), X-ray gas in clusters, (Bryan & Norman 1998), and large-scale structure (Bryan et al. 1999; O'Shea et al. 2015), and the epoch of reionization (Norman et al. 2015), among others. For simplicity, all simulations are run with fixed resolution.

The MHD equations with burning are as follows:

$$\frac{\partial \rho}{\partial t} + \nabla \cdot (\rho \boldsymbol{v}) = 0, \tag{1}$$

$$\frac{\partial \rho \boldsymbol{v}}{\partial t} + \nabla \cdot \left(\rho \boldsymbol{vv} + \boldsymbol{I}P - \frac{\boldsymbol{BB}}{8\pi} \right) = -\rho \boldsymbol{g}, \tag{2}$$

$$\frac{\partial E}{\partial t} + \nabla \cdot \left[(E + P)\boldsymbol{v} - \frac{\boldsymbol{B}(\boldsymbol{B} \cdot \boldsymbol{v})}{4\pi} \right] = -\rho \boldsymbol{v} \cdot \boldsymbol{g} + \dot{Q}, \tag{3}$$

$$\frac{\partial \boldsymbol{B}}{\partial t} + \nabla \times (\boldsymbol{v} \times \boldsymbol{B}) = 0, \tag{4}$$

where $\boldsymbol{vv}$ and $\boldsymbol{BB}$ are the velocity and the magnetic field outer products and ρ, $\boldsymbol{g}$, and $\dot{Q}$ are the density, the gravitational acceleration, and the energy production rate from the nuclear burning. The total energy density is equal to the total of the thermal, the kinetic and the magnetic energy densities,

$$E = e + \frac{\rho v^2}{2} + \frac{B^2}{8\pi}, \tag{5}$$

and

$$P = p + \frac{B^2}{8\pi} \tag{6}$$

is the total pressure, which is the thermal plus the magnetic pressure.

A particular realization of a degenerate relativistic equation of state (EOS) from Hoeflich (2006) is shown in Figure 4. Considering the right two panels, one can assume that at temperatures $T \gtrsim 10^{9.5}$ K and at densities in the range $\rho = 10^7$–10^8 g cm^{-3}, the adiabatic index $\gamma = $ const is a reasonable approximation. Hence, we close the system with the equations of state for an ideal gas,

$$e = \frac{p}{\gamma - 1}, \tag{7}$$
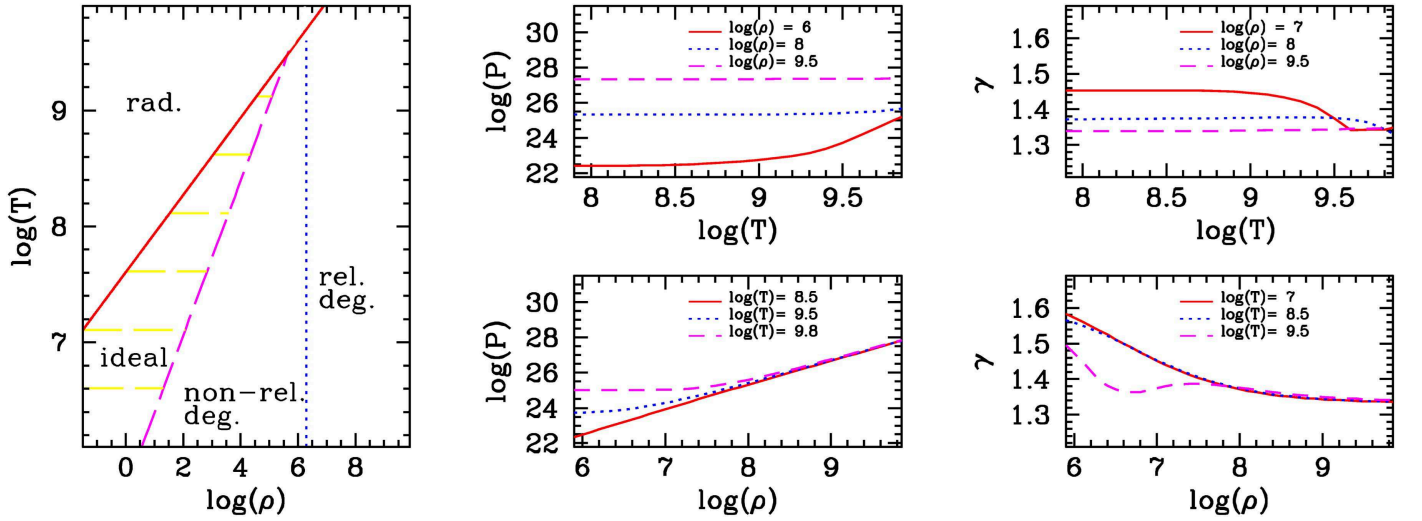
Figure 4. EOS of a WD (Hoeflich [2006](2006)). The two right panels show that γ depends relatively weakly on T and on ρ in the non-distributed regime of burning ($T \geqslant 10^{8.5}$ K and $\rho \sim 10^8$ g cm^{-3}), hence it can be taken to be a constant.

where the adiabatic index $\gamma = 1.4$ for these simulations.

2.3. Burning

We model the nuclear burning and flame propagation after Khokhlov ([1995](1995)), which takes advantage of the non-distributed regime in a couple of ways. First, it takes a grid resolution much coarser than the flame scale length, as discussed in Section [2.1.4](2.1.4). Then it approximates the real nuclear network with one that has only two elements:

$$\text{fuel} \rightarrow \text{product} + \mathcal{Q} \qquad (8)$$

where $\mathcal{Q}$ is the specific energy produced from burning. In our simulations the fuel consists of equal amounts by number of ^{12}C and ^{16}O with a mean atomic weight $\mathcal{A}_{\text{fuel}} \approx 14$, and the product is ^{56}Ni. We define the burned molar fraction, simply referred to as burned fraction, f, as

$$f = \frac{\mathcal{Y}_{\text{prod}}}{\mathcal{Y}_{\text{fuel}} + \mathcal{Y}_{\text{prod}}}, \qquad (9)$$

where $\mathcal{Y}_i$ are the abundances. Note that $f \in [0, 1]$, where $f = 0$ corresponds to pure fuel, and $f = 1$ means pure product. A nuclear deflagrating flame ignites unburned fuel by heating through electron conduction. The model flame spreads by diffusing the burned fraction, f:

$$\frac{\partial f}{\partial t} + \mathbf{v} \cdot \nabla f = K \nabla^2 f + R(f). \qquad (10)$$

Here, K approximates the diffusion of burning material and thus energy to ignite the upstream fuel. The instantaneous burning rate is then denoted by R. The front becomes stretched over a few grid cells, as is typical for shock-capturing schemes. The laminar speed velocity should be proportional to $\sqrt{KR}$. We chose a value of 10 km s^{-1}, which we confirmed in a 1D run. According to Remming & Khokhlov ([2016](2016)), the laminar front velocity depends on the magnetic field strength and direction, in addition to the fuel density. However, in our regime the difference the authors had calculated is about 3%, allowing us to assume constant values for K and R. Additionally, we turn R

on and off locally, depending on the burned fraction:

$$R = R(f) = \begin{cases} R_0, & \text{if } f_0 \leqslant f \leqslant 1; \\ 0, & \text{if } 0 \leqslant f < f_0 \end{cases} \qquad (11)$$

and $f_0 = 0.3$ as in Khokhlov ([1995](1995)).

This delays the ignition of the fuel locally, preventing the entire domain from been ignited in the first few time steps by non-physical numerical waves traveling faster than the physical laminar flame. Finally, the burning energy is calculated as

$$\dot{\mathcal{Q}} = \mathcal{Q} \frac{d\rho_{\text{prod}}}{dt}. \qquad (12)$$

3. Results

As described in Section [2](2), Figures [1](1) and [2](2) show the effect of magnetic field on the propagation of nuclear burning in our simulations. There is a clear impact of the magnetic field on the speed and morphology of the front in the strongest field simulations, but one can see that all of the tested fields leave some imprint on the burning front regardless of the initial magnitude or direction. At low magnetic field, ($B \lesssim 10^9$ G, and including no field at all, bottom row in those figures), the relative initial pressure (thus initial density) gradient is opposite to gravity, making the flow RT-unstable. Large modes grow faster, as expected, and they would continue to rise. The flame morphology becomes increasingly complex. The burning front develops chaotic structure and is dominated by turbulence. Small modes grow slower and are washed out by the flow shear or the diffusion by which the laminar front advances (Khokhlov [1995](1995), see also Equation ([10](10))) The effective front width is $\sim$50–70 km. Some pockets of fuel are formed.

Going up in magnitude to 10^{10} G, we can recognize a trend of the effective width of the burning front shrinking. This is most pronounced in the case of a transverse field. Turbulence is still prominent, and the front is comparable to that of the lower B cases.

At the highest magnetic field strengths, stabilization effects are well manifested. The chaotic behavior is suppressed, and the front structure is closer to laminar. The effective front width
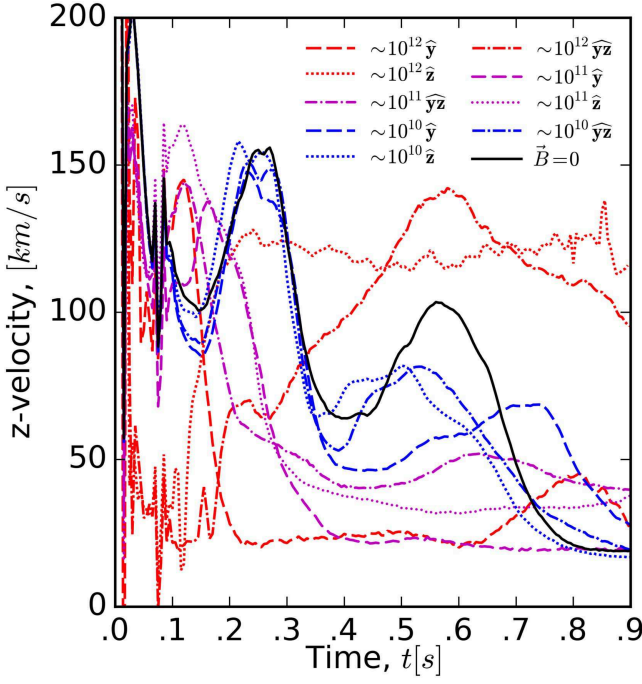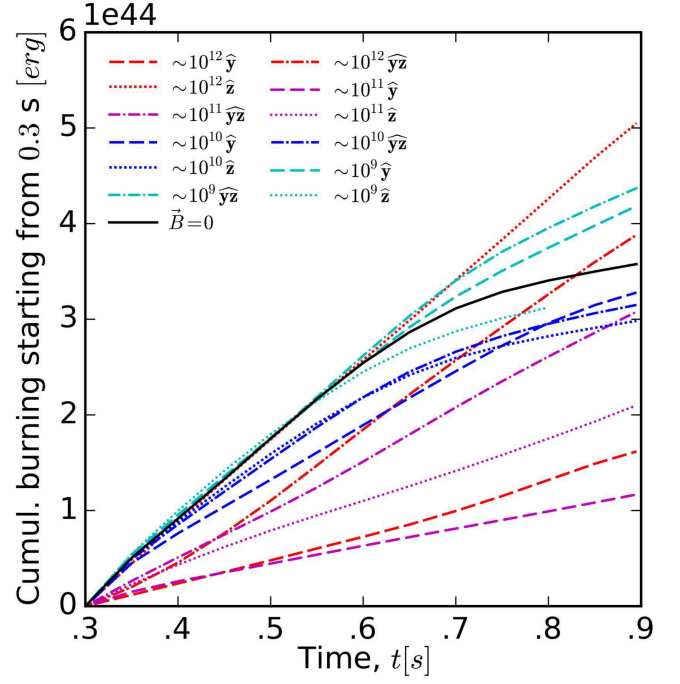
Figure 5. Flame speed in the frame comoving with the bulk flow. The 10^8 G and 10^9 G profiles are omitted for clarity. For most simulations, the velocity is decreased over the non-magnetized case by the reduction of the surface area of the front. The Z12 and YZ12 velocities are larger than any other case, as these regimes have a new kind of instability, as discussed in Section 3.2.

Figure 6. Cumulative burning energy, integrated from $t = 0.3$ s. The 10^8 G profile is not shown for clarity. In order to remove the effects of the initial conditions, seen in Figure 5, we integrate the burning rates starting right after the burst. We note a trend for the rates to drop with increasing field magnitude up to 10^{11} G. Beyond that models Z12 and YZ12 show the steepest slopes, as well as steady-state processes.
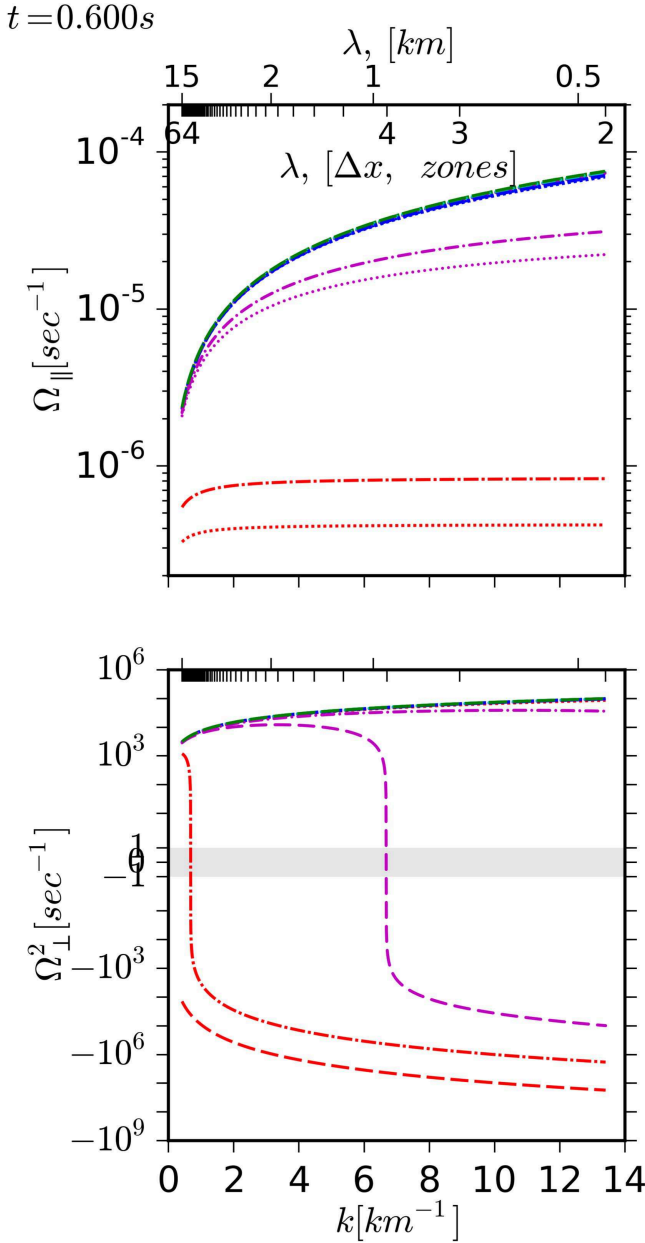
is now only on the order of 10 km. For models Y11, YZ11, and Y12 the flame front closely follows the field lines.

For models Z12 and YZ12 we identify another change in the behavior. The front becomes jagged with smaller peaks oriented along z. In YZ12 these are seen only in the y-projection. This behavior is mirrored in the front velocity and energy production, shown in Figures 5 and 6, respectively. In Figure 5, the black line shows the velocity of the fiducial un-magnetized run. After an initial transient phase, as the instability sets in prior to $t = 0.3$ s, it is clearly seen that the moderately magnetized runs (blue lines at 10^{10} G and purple lines at 10^{11} G) move slower due to the decreased surface area of the front. This decrease is also seen in the energy production rate, which can be seen as a proxy for the surface area; see Equation (11). In these runs, the instability is suppressed as expected by perturbation analysis, as discussed in Section 3.1. For the largest field runs that also contain a component along the propagation direction, however, the behavior is somewhat counterintuitive. These runs show a significant *increase* in the front velocity over all other runs. This is due to suppression of secondary Kelvin–Helmholtz instability; see Section 3.2.

3.1. Linear Stability Analysis

The MHD Equations (1)–(4) can be perturbed about an interface subject to an acceleration, and the growth rates calculated, as is done in standard Rayleigh–Taylor or Kelvin–Helmholtz instability studies. The magnetic field can exert tension in the front, and tend to stabilize the flow. Details are left to Appendix C, but we will discuss the salient results here. The analysis assumes that the magnetic field is either parallel or perpendicular to the gravity, g and the position of the front is assumed to behave as $\exp(ik_x x + ik_y y + \Omega t)$. Here, a negative Ω^2 indicates a stable mode. The dispersion relation for the field

perpendicular to g, presented in the bottom panel of Figure 7, shows that the only simulations with some stable modes in the linear regime are Y11, YZ11, and Y12. All other orientations, at all modes, remain unstable. This explains the stark contrast between the top two rows and the other four in Figures 1 and 2. Having stable modes above a certain magnetic field strength is an effect of the finite domain size, as mentioned in the beginning of Section 2.

When the field is parallel to the gravity, the top panel of Figure 7 shows no stable linear modes, regardless of the field strength. This not a limitation of the domain size or the resolution but works for all wavenumbers, as proved in Chandrasekhar (1961). We also note that the growth rate is monotonic with respect to the size of the perturbation, with the smallest modes growing fastest. However any of the calculated growth rates (considering all models, including $B = 0$) do not exceed 10^{-4}, which means that in this case the duration of the problem, ~ 1 s is too short for any linear perturbations to grow.

3.2. Nonlinear Growth

The linear stability is useful for guiding intuition, but the flow in question is no longer in the linear regime.
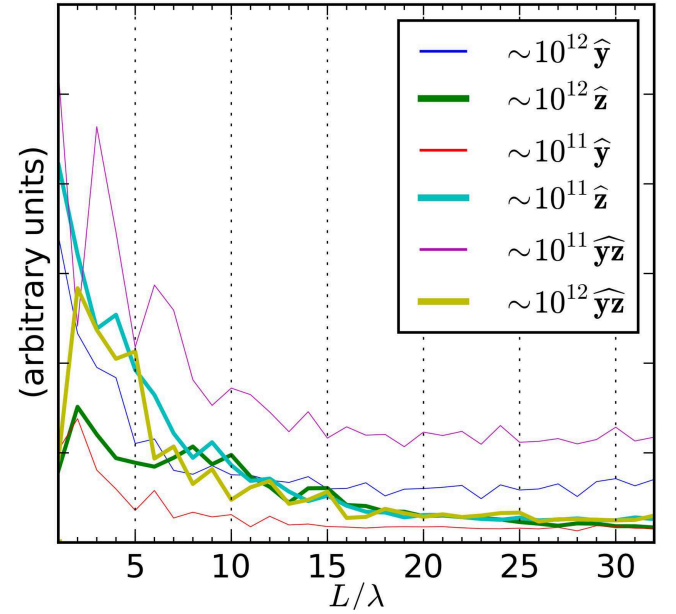
In order to quantify this impression we applied a Fourier transform to the 95% iso-surface of the burned fraction in all 10^{11} and 10^{12} runs, shown in Figure 8. This is a good method for the YZ12 and Z12 models, since the said iso-surface is a single-valued function, $\zeta(x, y)$. When the front has multiple points for the same (x, y) we take the rightmost one. Most profiles have the same power for the medium modes in the range $L/\lambda = 8\text{--}15$. However, these are dominated by the larger modes $(L/\lambda = 1\text{--}6)$ and appear as noise. The Z12 spectrum, on the other hand, shows suppressed large modes to

Figure 8. Fourier transformation of the flame as a function of *x* and *y* for the high-field simulations. All profiles are normalized so that they have maximum 1, in order to emphasize the distribution of power within each simulation, rather than comparing powers between simulations. The Z12 spectrum shows stronger features for $L/\lambda = 8$–15 compared to the rest. This is due to the lateral magnetic support against secondary instabilities once perturbations become elongated. Additionally, all profiles become flat for $L/\lambda \geqslant 16$ with little power in that region, i.e., only modes larger than two computational cells are prominent. This can be attributed to competition of advection vs. diffusion, but could be a resolution effect as well, and needs to be studied further.

Figure 7. Growth rate of perturbation modes. See the legend in Figure 6. Negative values indicate stable modes. The theoretical dispersion relations are used for magnetic fields parallel (Equations (18)–20), and perpendicular (Equation (21)) to *g* at *t* = 0.6 s. The wavelength range starts from two computational cells up to the entire domain width. For the perpendicular cases (bottom panel) we see that stable modes can be expected only in three simulations, whereas all modes are stable in the Y12 run. This is a rough agreement with the flows shown in Figure 1, especially in the $\hat{y}$ models. We also see stable surfaces along the magnetic field in the YZ11 run. In the parallel cases (top panel) none of the simulations show stable modes. and the smallest modes grow the fastest. However, the growth rate is suppressed so much that no growth will occur for the duration of the problem, ∼1 s.

the same level of power as the medium modes. Therefore, we cannot consider the latter as noise.

Furthermore, the side walls of these instabilities become almost parallel to $\hat{z}$, where the sinking fuel and the rising burned material create shear at the boundary. These conditions are ripe for developing Kelvin–Helmholtz instabilities, but the magnetic field is now almost parallel to the shear interface, adding tension and making the flow laterally stable. The

condition for Kelvin–Helmholtz stability, derived in the stability analysis in the Appendix (in Equation (22)) is visualized in a 1-zone slice in Figure 9. It holds for all zone boundaries parallel to $\hat{z}$. Somewhat similar effects to the RT fingers were observed by Stone & Gardiner (2007a, 2007b) in lateral direction caused by magnetic fields perpendicular to the gravity. Most importantly, they consider non-reactive fluids and observe bubble growth proportional to t^2. In our models, burning is expected to limit this growth in all regimes. Specifically, in the Z12 and YZ12 models, the height of the burning zone, once established, remains about the same throughout the simulation.

We also observe that all spectra become flat for $L/\lambda > 15$, with the least power in those modes. Since the lateral advection is suppressed we could attribute this effect to diffusion; however, it could be something else, including numerical.

Figure 9 shows fingers of fuel with a width comparable to the flame laminar thickness, 3–4 zones. Poludnenko & Oran (2011) and Hicks (2015) found that when the radius of curvature at the bottom of the fingers becomes on the order of the laminar flame thickness or less, the fuel burns at an accelerated rate. The plots in Figures 5 and 6 confirm this. We note that the burning rates and the front speeds tend to drop with magnitude and are smallest at about 10^{11} G due to the decrease of the front surface, but in the Z12 and YZ12 models the profiles become steeper again.

4. Discussion

We show that a magnetic field in the WD deflagration regime has an effect on nuclear burning for magnitudes $B \gtrsim 10^{10}$ G. At medium to high magnitudes we observe a front
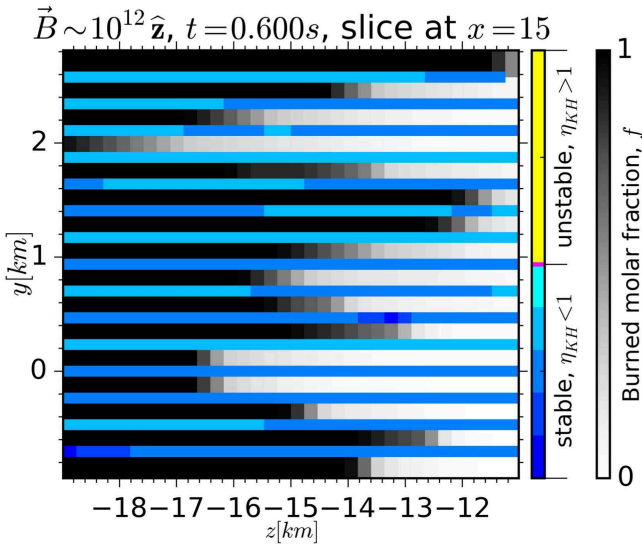
Figure 9. The "Kelvin–Helmholtz number" (Equation (22), yellow-to-blue scale) on the computational cell boundaries superimposed on the burned fraction (grayscale) for the Z12 model at $t = 0.6$ s. Cold fuel sinks against the rising burned material, creating shear on the vertical cell boundaries. All lateral perturbations, i.e., the secondary Kelvin–Helmholtz instabilities, are suppressed by the magnetic field, sustaining the finger formations.

that is more organized compared to low magnetic field strength or no field at all. The burning front becomes more laminar and less turbulent, and RT instabilities decrease. The effective front thickness also decreases by a factor of a few. One should ask whether medium fields are sufficient to bring significant change in the final outcome of the explosion, given that a Type Ia deflagration is estimated to only last about 2 s. The front speed and total burning rate tend to decrease as the field magnitude grows up to 10^{11} G, regardless of the field direction. Note that without steady-state flows it is not meaningful to compare models one-to-one. However, it is clear that the YZ12 and Z12 models have the fastest fronts and the effects of the direction of B are stronger. When the longitudinal component of the field is strong, the burning is amplified and the front speed is highest and larger than the pure hydrodynamical case by a factor of 3 to 4.

4.1. Impact of Magnetic Fields

These results suggest that strong magnetic fields might be missing from the picture of WD explosion physics painted by current 3D models. Suppression of large modes of RT instabilities in the early stages of the explosion is necessary to prevent large-scale mixing until the transition to detonation. A second possible implication is related to the development of small-scale structures that result in an effective increase in the "surface" of the flame, which is the physical underpinning for a significant increase of the burning rate compared to a pure hydrodynamical front. If burning rate is amplified by magnetic fields, it can lead to faster expansion and may freeze out the RT plumes in the unburned environment, consequently not allowing them to rise to the surface, which also means less mixing.

As discussed in the introduction, the delayed-detonation model is currently the favorite for M_{Ch} explosions, but DDT remains unexplained. Possible processes based on the Zel'dovich mechanism are still under discussion. In order to increase the nuclear burning rate and form a detonation front, these require simultaneous mixing of burned and unburned matter on

small scales over a significant volume. Possible physical causes for such mixing include mixing during a pulsational phase of the WD by crossing shock waves produced in the highly turbulent medium, shear flows, and instabilities in the regime of distributed burning, which are discussed in Poludnenko (2016). However, small-scale fluctuations may be expected to prevent a DDT through mixing (Khokhlov et al. 1997; Niemeyer & Woosley 1997). Another way to transition to detonation is by compression, when the speed of the burning front reaches the so called Chapman–Jougey limit. No solution for steady burning by deflagration exists above this limit, which for C/O rich mixtures is about 40% of v_s (Bruenn 1972). Based on 3D full-star simulations of deflagration fronts (e.g., Gamezo et al. 2003), pure deflagration fronts reach about 10%–15% effective burning speed if full-scale RT instabilities have developed over $\approx$2–3 s. In all simulations, detonation in hydrodynamical models needs to be triggered "by hand." The RT stabilization effect of magnetic fields should additionally reduce the front surface, and thus the front speed, leading to a decreased likelihood of DDT by either mechanism. Our results of small-scale structure with an effective increase of the burning by factors of 3–5 in the YZ12 and Z12 models may open an alternative mechanism for the DDT, as a similar factor in the regime of distributed burning would bring the burning speed well above the Chapman–Jougey limit. Because the structure depends on the size and orientation of B, we must expect a wide variety and a dependence of the field morphology. A final answer is beyond this paper and will be addressed in full-star simulations in future works.

4.2. Magnetic Field Growth and Saturation

We have shown that B fields larger than $10^{9\cdots10}$ G will have a significant effect on the nuclear burning fronts under WD conditions, and may solve some of the current problems with M_{Ch} explosions and delayed-detonation models in particular. As discussed in the introduction, some WD have magnetic fields but, for most WDs, the B fields are much smaller than those indicated by late-time observations of SNe Ia. Is it possible to produce high fields on relevant timescales prior to the explosion? Dynamos may be created during the accretion phase on timescales of 10^6 years, or during the smoldering phase leading to the thermonuclear runaway on timescales of minutes (Hoeflich & Stein 2002), or during the hydrodynamical phase of instabilities during the explosion on timescales of seconds or less. This leads us directly to B-field amplification in WDs and dynamo theories.

A seed magnetic field can be amplified by a dynamo operating in the convective zone of a differentially rotating star, including WDs (Parker 1979; Thomas et al. 1995; Brandenburg & Subramanian 2005). In large-scale dynamos, a toroidal field is produced by winding-up the poloidal component. The convective elements move upward and downward, perpendicular to the toroidal field lines, bending them and creating a new poloidal component (Parker 1979). Large-scale dynamos grow with a typical timescale of the Alfvén times, $t_A \approx R(4\pi\rho)^{1/2}/B \approx 300$ s (Parker 1979), which is comparable to the final phase prior to the runaway. Therefore, this is not sufficient to increase the field by several orders of magnitude.

Alternatively, in the *small-scale* dynamo, turbulence alone can amplify fields very quickly (Kazantsev 1968; Tayler 1973; Acheson 1978; Hawley et al. 1996; Spruit 2002; Brandenburg &

Subramanian 2005; Schekochihin & Cowley 2007; Beresnyak et al. 2009; Braithwaite 2009; Duez et al. 2010a, 2010b). Within the core of a white dwarf close to M_{Ch}, turbulence will undoubtedly play an enormous role. As the WD approaches M_{Ch}, the polytropic index, $\gamma \rightarrow 4/3$, and the stability against radial motion disappears. Then, kinetic energy will exhibit a Kolmogorov cascade, with energy distributed at all scales in a power law, $E = Ck^{-5/3}$. This power law persists to the molecular viscous dissipation scale. Initially weak magnetic fields are stretched, twisted, and folded to increase the strength of the field. This mechanism will cause amplification until the kinetic and magnetic energies at a given scale are equal. In the *kinematic phase*, the magnetic energy is significantly below the kinetic energy. This occurs for large scales (small wavenumber) $k < k^*$, where the equipartition scale, k^*, is determined by the scale at which amplification is balanced by dissipation and transfers to higher scales. For small scales (large wavenumber), $k > k^*$, the magnetic field follows a Kolmorgorov cascade. The equipartition wavenumber, k^*, then decreases linearly with time (Schekochihin & Cowley 2007; Beresnyak et al. 2009).

The details of this dynamo depend on the kinetic and magnetic dissipation scales. The kinematic viscosity and magnetic diffusivity have been found to be $\nu = 3.13 \times 10^{-2}$ cm^2 s^{-1} and $\eta = 5.6 \times 10^{-2}$ cm^2 s^{-1}, respectively (Nandkumar & Pethick 1984; Isern et al. 2017). With a typical velocity and length of $V \simeq 16$ km s^{-1} and $L \simeq 200$ km, respectively (e.g., Nonaka et al. 2012), we find kinetic and magnetic Reynolds numbers of Re $\equiv LV/\nu = 10^{15}$ and Rm $\equiv LV/\eta = 5 \times 10^{14}$, respectively. We also find viscous and magnetic length scales of $\ell_\nu = L$ Re$^{-3/4} = 10^{-4}$ cm and $\ell_\eta = 1.7 \times 10^{-4}$ cm. Behavior of the turbulent dynamo depends on the magnetic Prandtl number, Pm $= \nu/\eta = 0.5$ for this system. In recent theoretical studies (e.g., Schekochihin & Cowley 2007; Beresnyak et al. 2009; Schober et al. 2012), it has been shown that the field can grow to energy equipartition at a given scale in an eddy turnover time at the smallest scale, essentially instantaneously, during the kinematic phase. Schober et al. (2012) estimated this growth rate for both large and small Pm, finding that the growth rate $\Gamma = 0.027$Rm$^{1/2}V/L$, for low values of Pm. Conservative estimates for the L, V and Pm given above yield a growth rate of 5×10^4 s^{-1}, or a doubling time of 2×10^{-5} s. Using length and velocity scales more appropriate for later phases of the WD (e.g., Hoeflich & Stein 2002), $V \simeq 200$ km s^{-1} and $L \simeq 100$ km, we find $\Gamma = 3 \times 10^6$ s^{-1}.

It has been estimated (Schekochihin & Cowley 2007) that the timescale for the equipartition length scale, $1/k^*$, to reach the outer scale of the turbulence, L, is $t = L/U$. For our first estimate, this is 12 s, while for our second it is 0.5 s. To estimate the final level of magnetic field when the dynamo ceases to function, Schober et al. (2015) examine the feedback mechanism of Subramanian (1999). In this model, the magnetic diffusivity increases with magnetic energy. These authors find that in the small magnetic diffusivity limit, as much as 40% of the total kinetic energy can be converted to magnetic energy. This is similar to numerical findings; for example, Haugen et al. (2004) found 30% of the energy is magnetic, Cho & Vishniac (2000) found 25%, and Beresnyak (2014) found 15%. If the peak magnetic energy is some fraction, f, of the total,

$$\frac{B^2}{8\pi} = f\frac{1}{2}\rho V^2,$$

and $\rho = 10^9$ g cm^{-3} and $f = 0.4$, we find a field of 10^{11} G and 1.4×10^{12} G for the two conditions above. In a recent success of both laboratory plasma physics and theory, Tzeferacos et al. (2018) used the Omega laser facility at the University of Rochester to produce a 102 kG magnetic field. They found a value of the ratio of magnetic energy to kinetic energy of $f = 0.04$, which is somewhat lower than the numerical results, but will still result in a substantial magnetic field in a WD. Ultimately, the details of the evolution depend on the details of the simulation, so full white dwarf simulations will be needed to specify the field for this specific system.

4.3. Future Work

We want to emphasize that this study presents only a first step toward addressing the MHD problem for reactive fluids. Firm conclusions for an exploding WD require many more questions to be addressed. Here, we will mention the limits of this study and questions which will be addressed in the near future by full-star models with our existing, more detailed nuclear networks. First, we treat the problem as if the WD was not expanding during the simulation—our gravitational acceleration is a constant instead of decreasing with time. Radial gradients in the gravitational acceleration, the initial density, and the initial pressure were neglected. Furthermore, an evolved magnetic field would not be uniform, so the flame will encounter varying magnitude and direction as it advances. Moreover, the laminar diffusion speed will become directionally dependent. These effects will be studied in flux tubes using our Monte-Carlo transport coupled within a Particle in a Cell scheme. Finally, our nuclear network is too simple to carry out simulations in a distributed regime of burning should one want to include the detonation phase as well.

High resolution simulations of a full star are required in order to overcome the limitations of the flux tube results presented in this work. Other scientific questions we want to address in the future are as follows. Are magnetic fields the missing physics in the current 3D models? In particular, do magnetic fields make pre-expansion of the WD possible; and if so, what is the mechanism—is it by suppressing the RT instabilities, by plume freeze-out on an accelerated background, or in some other way? What are observational signatures of the different field magnitudes and morphologies? Can they lead to different outcomes of the explosions, i.e., can different magnetic fields explain some of the diversity of SNe Ia?

Computing Center (https://rcc.fsu.edu), for help with technical problems. Visualization was done using yt (Turk et al. 2011), matplotlib (Hunter 2007), and numpy (van der Walt et al. 2011). We thank Nathan Goldbaum and Matthew Turk for help on yt issues.

Appendix A
Mass and Molar Fraction Definitions and Identities

Here, we define some quantities used in the text and give some conversions between them. Consider the fuel and product mixture, which we shall label with 1 and 2, respectively, to ease the notation. The partial mass densities add up to the total mass density:

$$\rho = \rho_1 + \rho_2. \tag{13}$$

We then define the mass, the molar, and the burned fractions, $\mathcal{X}$, $\mathcal{Y}$, and f:

$$\mathcal{X}_i \equiv \rho_i/\rho, \quad \mathcal{Y}_i \equiv \mathcal{X}_i/\mathcal{A}_i, \tag{14}$$

$$f \equiv \frac{\mathcal{Y}_2}{\mathcal{Y}_1 + \mathcal{Y}_2}. \tag{15}$$

Clearly, the burned and the fuel fractions comprise the entirety of the material, i.e., the fuel fraction equals to $1 - f$, should one need it.

Using the definitions above it is easy to derive the following identities. The first two express the burned fraction, f, in terms of the total mass density, ρ, and one of the partial mass densities, ρ_1 or ρ_2. The following two equations show how to calculate the abundances, $\mathcal{Y}_{1,2}$, from the burned fraction, f.

$$f = \frac{\mathcal{A}_1(\rho - \rho_1)}{\mathcal{A}_1\rho - (\mathcal{A}_1 - \mathcal{A}_2)\rho_1} = \frac{\mathcal{A}_1\rho_2}{\mathcal{A}_2\rho + (\mathcal{A}_1 - \mathcal{A}_2)\rho_2}, \tag{16}$$

$$\mathcal{Y}_1 = \frac{1 - f}{\mathcal{A}_1(1 - f) + \mathcal{A}_2 f}, \mathcal{Y}_2 = \frac{f}{\mathcal{A}_1(1 - f) + \mathcal{A}_2 f}. \tag{17}$$

Appendix B
Burning Operator

Provided that we know ρ, from Equations (13) and (16), it follows that we only need the mass fraction and one of the partial mass densities to determine the other one. In our implementation of the new burning operator in Enzo, it is the product mass density, ρ_2, that is being stored and advected. The burning operator comes last in the time cycle and comprises the following steps:

(i) find the burned fraction at the beginning of the cycle, using the second part of Equation (16);
(ii) evolve the burned fraction using a 27-point stencil for the Laplacian;
(iii) update the density from Equation (17); and
(iv) update the energy from Equation (12).

Appendix C
Linear Stability Theory

We use analytic linear stability results from Chandrasekhar (1961). These come from linear stability analyses of the growth rate, Ω, of normal perturbation modes, $\mathbf{k} \equiv k_x \hat{\mathbf{i}} + k_y \hat{\mathbf{j}}$, along the discontinuity interface, so that a perturbation is proportional

to $\exp(ik_x x + ik_y y + \Omega t)$. Modes with such dependence on time are stable when $\Omega^2 < 0$.

We split the magnetic field into two terms, parallel and perpendicular to the gravity, i.e., $\mathbf{B} \equiv B_z \hat{\mathbf{k}} + \mathbf{B}_\perp$, where $B_z \neq 0$ and $\mathbf{B}_\perp \equiv B_x \hat{\mathbf{i}} + B_y \hat{\mathbf{j}} \neq 0$, respectively. The dimensionless dispersion relation for B_z is

$$\eta^3 + 2\kappa(\alpha_2^{1/2} + \alpha_1^{1/2})\eta^2 + \kappa(2\kappa + \alpha_1 - \alpha_2)\eta$$
$$- 2\kappa^2(\alpha_2^{1/2} - \alpha_1^{1/2}) = 0, \tag{18}$$

where

$$\eta \equiv \frac{\Omega_\parallel}{g/V_{A,z}}, \quad \kappa \equiv \frac{k_\parallel}{g/V_{A,z}^2}, \tag{19}$$

$$V_{A,z}^2 \equiv \frac{B_z^2}{4\pi(\rho_2 + \rho_1)}, \quad \alpha_{1,2} \equiv \frac{\rho_{1,2}}{\rho_1 + \rho_2}, \tag{20}$$

and $\rho_1 < \rho_2$. In this case no values of the parameters B and $\rho_{1,2}$ yield stable modes.

We rewrite the dispersion relation for $\mathbf{B}_\perp$, for the modes parallel to the magnetic field, $\mathbf{k}_\perp \parallel \mathbf{B}_\perp$. Modes not parallel to $\mathbf{B}_\perp$ are "less" stable since the negative term should be multiplied by $\cos^2(\mathbf{B}_\perp, \mathbf{k}_\perp)$.

$$\Omega_\perp^2 = gk_\perp \left(\frac{\rho_2 - \rho_1}{\rho_2 + \rho_1} - \frac{B_\perp^2}{2\pi(\rho_2 + \rho_1)g}k_\perp \right). \tag{21}$$

Modes are stable when the right side of Equation (21) is negative.

Finally, we rewrite the condition for a mode to be Kelvin–Helmholtz stable as

$$\eta_{KH} \equiv \frac{\alpha_1\alpha_2 \Delta v_z}{2\eta_{KH}} < 1. \tag{22}$$

ORCID iDs

David C. Collins ⓘ https://orcid.org/0000-0001-6661-2243
Peter Hoeflich ⓘ https://orcid.org/0000-0002-4338-6586
Tiara R. Diamond ⓘ https://orcid.org/0000-0002-0805-1908

References

Abel, T., Bryan, G. L., & Norman, M. L. 2002, Sci, 295, 93
Acheson, D. J. 1978, RSPTA, 289, 459
Alvear Terrero, D., Castillo García, M., Manreza Paret, D., Horvath, J. E., & Pérez Martínez, A. 2015, AN, 336, 851
Badenes, C., Borkowski, K., Hughes, J., Hwang, U., & Bravo, E. 2006, ApJ, 645, 1373
Barbon, R., Benetti, S., Rosino, L., Cappellaro, E., & Turatto, M. 1990, A&A, 237, 79
Benz, W., Cameron, A. G. W., Press, W. H., & Bowers, R. L. 1990, ApJ, 348, 647
Beresnyak, A. 2014, ApJL, 784, L20
Beresnyak, A., Jones, T. W., & Lazarian, A. 2009, ApJ, 707, 1541
Braithwaite, J. 2009, MNRAS, 397, 763
Brandenburg, A., & Subramanian, K. 2005, PhR, 417, 1
Bruenn, S. W. 1972, ApJ, 177, 459
Bryan, G. L., Machacek, M., Anninos, P., & Norman, M. L. 1999, ApJ, 517, 13
Bryan, G. L., & Norman, M. L. 1998, ApJ, 495, 80
Bryan, G. L., Norman, M. L., O'Shea, B. W., et al. 2014, ApJS, 211, 19
Chandrasekhar, S. 1961, Hydrodynamic and Hydromagnetic Stability (Oxford: Clarendon)
Cho, J., & Vishniac, E. T. 2000, ApJ, 538, 217
Collins, D. C., Kritsuk, A. G., Padoan, P., et al. 2012, ApJ, 750, 13

Collins, D. C., Xu, H., Norman, M. L., Li, H., & Li, S. 2010, ApJS, 186, 308
Diamond, T. R., Hoeflich, P., & Gerardy, C. L. 2015, ApJ, 806, 107
Duez, M. D., Foucart, F., Kidder, L. E., Ott, C. D., & Teukolsky, S. A. 2010a, CQGra, 27, 114106
Duez, V., Braithwaite, J., & Mathis, S. 2010b, ApJL, 724, L34
Ferrario, L., de Martino, D., & Gänsicke, B. T. 2015, SSRv, 191, 111
Fesen, R. A., Hoeflich, P. A., Hamilton, A. J. S., et al. 2007, ApJ, 658, 396
Fesen, R. A., Höflich, P. A., & Hamilton, A. J. S. 2015, ApJ, 804, 140
Fisher, A., Branch, D., Nugent, P., & Baron, E. 1997, ApJL, 481, L89
Foley, R. J., Challis, P. J., Chornock, R., et al. 2013, ApJ, 767, 57
Franzon, B., & Schramm, S. 2017, JPhCS, 861, 012015
Gamezo, V. N., Khokhlov, A. M., & Oran, E. S. 2005, ApJ, 623, 337
Gamezo, V. N., Khokhlov, A. M., Oran, E. S., Ctchelkanova, A. Y., & Rosenberg, R. O. 2003, Sci, 299, 77
Gardiner, T. A., & Stone, J. M. 2005, JCoPh, 205, 509
Ghezzi, C. R., de Gouveia Dal Pino, E. M., & Horvath, J. E. 2001, ApJL, 548, L193
Ghezzi, C. R., de Gouveia Dal Pino, E. M., & Horvath, J. E. 2004, MNRAS, 348, 451
Giammichele, N., Bergeron, P., & Dufour, P. 2012, ApJS, 199, 29
Haugen, N. E., Brandenburg, A., & Dobler, W. 2004, PhRvE, 70, 016308
Hawley, J. F., Gammie, C. F., & Balbus, S. A. 1996, ApJ, 464, 690
Hicks, E. P. 2015, ApJ, 803, 72
Hoeflich, P. 1995, ApJ, 443, 89
Hoeflich, P. 2006, NuPhA, 777, 579
Hoeflich, P., Gerardy, C. L., Fesen, R. A., & Sakai, S. 2002, ApJ, 568, 791
Hoeflich, P., Gerardy, C. L., Nomoto, K., et al. 2004, ApJ, 617, 1258
Hoeflich, P., Hsiao, E. Y., Ashall, C., et al. 2017, ApJ, 846, 58
Hoeflich, P., & Khokhlov, A. 1996, ApJ, 457, 500
Hoeflich, P., & Stein, J. 2002, ApJ, 568, 779
Höflich, P., Gerardy, C. L., Marion, H., & Quimby, R. 2006, NewAR, 50, 470
Howell, D. A., Hoeflich, P., Wang, L., & Wheeler, J. C. 2001, ApJ, 556, 302
Howell, D. A., Sullivan, M., Nugent, P. E., et al. 2006, Natur, 443, 308
Hoyle, F., & Fowler, W. A. 1960, ApJ, 132, 565
Hristov, B., Collins, D. C., Hoeflich, P., & Weatherford, C. 2016, in AAS Meeting 227 Abstracts, 237.16
Hunter, J. D. 2007, CSE, 9, 90
Iben, I., Jr., & Tutukov, A. V. 1984, ApJS, 54, 335
Isern, J., García-Berro, E., Külebi, B., & Lorén-Aguilar, P. 2017, in ASP Conf. Ser. 509, 20th European White Dwarf Workshop, ed. P.-E. Tremblay, B. Gänsicke, & T. Marsh (San Francisco, CA: ASP), 409
Isern, J., Hernanz, M., & José, J. 2011, in Lecture Notes in Physics, Vol. 812, ed. R. Diehl, D. H. Hartmann, & N. Prantzos (Berlin: Springer), 233
Ji, S., Fisher, R. T., García-Berro, E., et al. 2013, ApJ, 773, 136
Kawka, A., Vennes, S., Schmidt, G. D., Wickramasinghe, D. T., & Koch, R. 2007, ApJ, 654, 499
Kazantsev, A. P. 1968, JETP, 26, 1031
Kepler, S. O., Pelisoli, I., Jordan, S., et al. 2013, MNRAS, 429, 2934
Kepler, S. O., Pelisoli, I., Koester, D., et al. 2016, MNRAS, 455, 3413
Kerzendorf, W. E., McCully, C., Taubenberger, S., et al. 2017, MNRAS, 472, 2534
Khokhlov, A. M. 1995, ApJ, 449, 695
Khokhlov, A. M., Oran, E. S., & Wheeler, J. C. 1997, ApJ, 478, 678
Kirshner, R. P., Jeffery, D. J., Leibundgut, B., et al. 1993, ApJ, 415, 589
Kritsuk, A. G., Norman, M. L., Padoan, P., & Wagner, R. 2007, ApJ, 665, 416
Kromer, M., Sim, S. A., Fink, M., et al. 2010, ApJ, 719, 1067
Kutsuna, M., & Shigeyama, T. 2012, ApJ, 749, 51
Li, S., Li, H., & Cen, R. 2008, ApJS, 174, 1
Li, W., Bloom, J. S., Podsiadlowski, P., et al. 2011, Natur, 480, 348
Li, W., Filippenko, A. V., Chornock, R., & Jha, S. 2003, PASP, 115, 844
Liebert, J., Bergeron, P., & Holberg, J. B. 2003, AJ, 125, 348
Livne, E. 1990, ApJL, 354, L53
Livne, E. 1999, ApJL, 527, L97
Lorén-Aguilar, P., Isern, J., & García-Berro, E. 2009, A&A, 500, 1193
Maeda, K., Benetti, S., Stritzinger, M., et al. 2010, Natur, 466, 82
Maeda, K., Leloudas, G., Taubenberger, S., et al. 2011, MNRAS, 413, 3075
Marion, G. H., Hoeflich, P., Vacca, W. D., & Wheeler, J. C. 2003, ApJ, 591, 316
Maund, J. R., Hoeflich, P. A., Patat, F., et al. 2010, ApJL, 725, L167
Mignone, A. 2007, JCoPh, 225, 1427
Milne, P., The, L.-S., & Leising, M 1999, ApJS, 124, 503
Motohara, K., Maeda, K., Gerardy, C. L., et al. 2006, ApJL, 652, L101
Nandkumar, R., & Pethick, C. J. 1984, MNRAS, 209, 511
Niemeyer, J. C., & Hillebrandt, W. 1995, ApJ, 452, 769
Niemeyer, J. C., & Woosley, S. E. 1997, ApJ, 475, 740
Nomoto, K. 1982a, ApJ, 257, 780
Nomoto, K. 1982b, ApJ, 253, 798
Nonaka, A., Aspden, A. J., Zingale, M., et al. 2012, ApJ, 745, 73
Norman, M. L., Reynolds, D. R., So, G. C., Harkness, R. P., & Wise, J. H. 2015, ApJS, 216, 16
O'Shea, B. W., Wise, J. H., Xu, H., & Norman, M. L. 2015, ApJL, 807, L12
Pakmor, R., Hachinger, S., Röpke, F. K., & Hillebrandt, W. 2011, A&A, 528, A117
Parker, E. N. 1979, Cosmical Magnetic Fields: Their Origin and Their Activity (New York: Oxford Univ. Press)
Patat, F., Hoeflich, P., Baade, D., et al. 2012, A&A, 545, A7
Penney, R., & Hoeflich, P. 2014, ApJ, 795, 84
Phillips, M. M. 1993, ApJL, 413, L105
Piersanti, L., Gagliardi, S., Iben, I., Jr., & Tornambé, A. 2003, ApJ, 598, 1229
Plewa, T. 2007, ApJ, 657, 942
Poludnenko, A. 2016, in Handbook of Supernovae, ed. P. Murdin (Berlin: Springer), 999
Poludnenko, A. Y., & Oran, E. S. 2011, arXiv:1106.3698
Potekhin, A. Y., & Chabrier, G. 2012, A&A, 538, A115
Pskovskii, I. P. 1977, SvA, 21, 675
Rasio, F. A., & Shapiro, S. L. 1994, ApJ, 432, 242
Reinecke, M., Hillebrandt, W., & Niemeyer, J. C. 1999, A&A, 347, 739
Reinsch, K., Euchner, F., Beuermann, K., Jordan, S., & Gänsicke, B. T. 2005, in ASP Conf. Ser. 330, The Astrophysics of Cataclysmic Variables and Related Objects, ed. J.-M. Hameury & J.-P. Lasota (San Francisco, CA: ASP), 177
Remming, I. S., & Khokhlov, A. M. 2014, ApJ, 794, 87
Remming, I. S., & Khokhlov, A. M. 2016, ApJ, 831, 162
Rest, A., Matheson, T., Blondin, S., et al. 2008, ApJ, 680, 1137
Rest, A., Suntzeff, N. B., Olsen, K., et al. 2005, Natur, 438, 1132
Röpke, F. K., Gieseler, M., Reinecke, M., Travaglio, C., & Hillebrandt, W. 2006, A&A, 453, 203
Röpke, F. K., Kromer, M., Seitenzahl, I. R., et al. 2012, ApJL, 750, L19
Schekochihin, A. A., & Cowley, S. C. 2007, in Turbulence and Magnetic Fields in Astrophysical Plasmas, ed. S. Molokov, R. Moreau, & H. K. Moffatt (Dordrecht: Springer), 85
Schober, J., Schleicher, D., Bovino, S., & Klessen, R. S. 2012, PhRvE, 86, 066412
Schober, J., Schleicher, D. R. G., Federrath, C., Bovino, S., & Klessen, R. S. 2015, PhRvE, 92, 023010
Segretain, L., Chabrier, G., & Mochkovitch, R. 1997, ApJ, 481, 355
Sion, E. M., Holberg, J. B., Oswalt, T. D., et al. 2014, AJ, 147, 129
Spruit, H. C. 2002, A&A, 381, 923
Stehle, M., Mazzali, P. A., Benetti, S., & Hillebrandt, W. 2005, MNRAS, 360, 1231
Stone, J. M., & Gardiner, T. 2007a, Physics of Fluid Dynamics Letters, 19, 094104
Stone, J. M., & Gardiner, T. 2007b, ApJ, 671, 1726
Stritzinger, M. D., Hsiao, E., Valenti, S., et al. 2014, A&A, 561, A146
Subramanian, K. 1999, PhRvL, 83, 2957
Sugimoto, D., & Nomoto, K. 1980, SSRv, 25, 155
Tanaka, M., Mazzali, P. A., Stanishev, V., et al. 2011, MNRAS, 410, 1725
Tayler, R. J. 1973, MNRAS, 161, 365
Thomas, J. H., Markiel, J. A., & van Horn, H. M. 1995, ApJ, 453, 403
Timmes, & Woosley 1992, ApJ, 396, 649
Turk, M. J., Smith, B. D., Oishi, J. S., et al. 2011, ApJS, 192, 9
Tzeferacos, P., Rigby, A., Bott, A. F. A., et al. 2018, NatCo, 9, 591
van der Walt, S., Colbert, S. C., & Varoquaux, G. 2011, in Société Royale des Sciences de Liége, Bulletin, Vol. 80, ed. G. Rauw et al., 260
Wang, B., Chen, X., Meng, X., & Han, Z. 2009a, ApJ, 701, 1540
Wang, B., Meng, X., Chen, X., & Han, Z. 2009b, MNRAS, 395, 847
Weaver, T. A., & Woosley, S. E. 1980, in AIP Conf. Proc. 63, Supernova models and light curves, ed. H. C. Wolfe, R. E. Meyerott, & G. A. Gillepsie (Melville, NY: AIP), 15
Webbink, R. F. 1984, ApJ, 277, 355
Whelan, J., & Iben, I. J. 1973, ApJ, 186, 1007
Woosley, S. E., & Kasen, D. 2011, ApJ, 734, 38
Woosley, S. E., & Weaver, T. A. 1994, ApJ, 423, 371
Yang, Y., Wang, L., Baade, D., et al. 2017, ApJ, 834, 60
Yoon, S.-C., Podsiadlowski, P., & Rosswog, S. 2007, MNRAS, 380, 933
Zhu, C., Pakmor, R., van Kerkwijk, M. H., & Chang, P. 2015, ApJL, 806, L1